Supporting Information

Ultrafast Interfacial Charge Transfer Drives Photocatalysis in Heterojunctions Between Nitrogen-rich Graphitic Carbon Nitride (g-C_3N_5) and Amino-Functionalized Carbon Quantum Dots

Pratibha Saini,[†*a] Arindam Konar,[†a,b] Ahmed Mansour,[a] Desirée Leistenschneider,[c,d] Marius Hermesdorf,[c] Sarah Jasmin Finkelmeyer,[b] Martin Presselt,[b,d,e] Martin Oschatz [c,d,f] and Benjamin Dietzek-Ivanšić*[a,b,g]

[a] *Institute for Physical Chemistry, Friedrich Schiller University Jena, Helmholtzweg 4, 07743 Jena, Germany. Email: sainip082@gmail.com, benjamin.dietzek-ivansic@iom-leipzig.de*
[b] *Department Functional Interfaces, Leibniz Institute of Photonic Technology (Leibniz-IPHT), Albert-Einstein-Strasse 9, 07745 Jena, Germany.*
[c] *Institute for Technical Chemistry and Environmental Chemistry, Friedrich Schiller University Jena, Philosophenweg 7a, 07743 Jena, Germany.*
[d] *Center for Energy and Environmental Chemistry Jena (CEEC Jena), Friedrich Schiller University Jena, Philosophenweg 7a, 07743 Jena, Germany.*
[e] *Sciclus GmbH & Co. KG, Moritz-von-Rohr-Str. 1a, 07745 Jena, Germany.*
[f] *Helmholtz Institute for Polymers in Energy Applications Jena (HIPOLE Jena), Lessingstraße 12–14, 07743 Jena, Germany.*
[g] *Leibniz Institute of Surface Engineering (Leibniz-IOM), Permoserstraße 15, 04318 Leipzig, Germany.*
[†] These authors contributed equally to this work.

Experimental Section

Materials

All chemicals and reagents were of analytical grade and used without further purification. Deionized water was used throughout the experiments.

Synthesis of bulk g-C_3N_5

Bulk triazole-based g-C_3N_5 nanomaterials were synthesized using 3-amino-1,2,4-triazole (3-AT) as the precursor.[1] A total of 6 g of 3-AT was ground into a uniform solid and transferred to an alumina crucible with a cover. The crucible was wrapped with a double layer of aluminum foil to limit direct exposure to atmospheric oxygen, placed in a muffle furnace, and heated at 500 °C for 3 hours, with a ramp rate of 8 °C min^{-1}. After natural cooling, the resulting brown material was collected, thoroughly washed several times with deionized water and ethanol, dried, and ground into a fine powder for further use and characterization, labelled as g-C_3N_5. The possible mechanism for the formation of this N-rich g-C_3N_5 is depicted in Scheme S1.[2]

Synthesis of conventional g-C_3N_4

Conventional carbon nitride was prepared using melamine as the starting material. A 5 g portion of melamine was placed in an alumina crucible covered with aluminum foil. The sample was heated to 500 °C in a tube furnace at a rate of 8 °C min^{-1} and held at that temperature for 3 hours. The resulting yellow product was then ground into a fine powder, referred to as g-C_3N_4.[3]

Synthesis of amino-rich-carbon quantum dots (AR-CQDs)

The synthesis of amine-rich carbon quantum dots (AR-CQDs) in this study follows the carbonization protocol developed in our previous work.[4-7] Trichosanthes dioica (Parwal) was first chopped, then dried, and subsequently heated in a muffle furnace at 300 °C for 3 hours before being ground into a fine powder. 100 mg of this powder was dispersed in 100 mL ultrapure water using ultrasonic treatment. The resulting black suspension was centrifuged at 12000 rpm for 15 minutes and filtered through a 0.22 µm membrane. The supernatant appeared brown in daylight and emitted green fluorescence under 365 nm UV light, indicating the formation of water-soluble AR-CQDs.

Synthesis of AR-CQDs/g-C_3N_5

AR-CQDs/g-C_3N_5 was synthesized through an ultrasound-assisted hydrothermal method. First, 3 g of bulk g-C_3N_5 powder was dispersed in 60 mL of the AR-CQDs solution (1 mg mL^{-1}), and the mixture was subjected to ultrasonication for 5 hours at room temperature to achieve a uniform suspension. This suspension was then transferred to a 100 mL Teflon-lined autoclave, sealed, and heated at 150 °C for 20 hours. After cooling, the final AR-CQDs/g-C_3N_5

(2 wt%) was collected *via* centrifugation, washed thoroughly several times with water and ethanol, and dried in a vacuum at 80 °C for 12 hours. For comparison, a process-matched control was prepared by subjecting bulk g-C_3N_5 to the same ultrasound-assisted hydrothermal treatment described above, but without adding AR-CQDs; the resulting material is denoted g-C_3N_5-HT.

Preparation of suspensions of g-C_3N_5, AR-CQDs, and AR-CQDs/g-C_3N_5 for spectroscopy measurements

The resulting powders from the synthesis of g-C_3N_5, AR-CQDs, and AR-CQDs/g-C_3N_5 were dispersed in distilled water and subjected to ultrasonication for 1 hour to ensure homogeneous suspension. The supernatant was collected after sedimentation and used for all spectroscopic measurements. For steady-state and time-resolved spectroscopic studies, the stock suspensions were further diluted to appropriate concentrations as required for each experimental setup.

Preparation of thin films using the drop-casting method

Thin films of g-C_3N_5, AR-CQDs, and AR-CQDs/g-C_3N_5 were prepared *via* a drop-casting technique. Initially, solutions of g-C_3N_5, AR-CQDs, and the AR-CQDs/g-C_3N_5 with a concentration of 1 g L^{-1} were prepared from the respective stock solutions. A measured volume of the prepared solutions was drop-cast onto thoroughly cleaned indium tin oxide (ITO) glass substrates to achieve uniform film coverage for reproducible and consistent optical measurements. The coated substrates were then dried in a laboratory oven at 60 °C overnight.

Characterization methods

Powder X-ray diffraction (XRD) was performed on a STOE Stadi P diffractometer, Darmstadt including a Ge-monochromator, a long fine focus Cu-tube and, a generator of 40 KV, 40 mA, and the position-sensitive detector (step = 2.1, with 60s per step). Fourier transform infrared (FT-IR) spectra was recorded using a Bruker Tensor 27 FT-IR spectrophotometer using a diamond ATR unit for solids with selected absorptions being recorded in the range of 4000-400 cm^{-1}. Electron paramagnetic resonance (EPR) spectra were recorded at room temperature in 4 mm quartz tubes using an X-Band ESR-ELEXSYS E580 spectrometer from Bruker quipped with an SHQE resonator (Bruker ER4122SHQE) at a microwave frequency of 9.87 GHz. The morphology of samples was observed using a JSM 6700F scanning electron microscope (SEM). For the SEM and energy dispersive X-ray spectroscopy (EDX) measurements the samples were suspended in ethanol, dropped on silicon substrates and coated with 5 nm of carbon. The SEM images were done with an accelerating voltage of 3 kV by using two different SE-detectors (TLD for perpendicular view and ETD for sample tilt of 30°). Transmission electron microscopy (TEM) images were obtained using a Hitachi HT7820 transmission electron microscope. Elemental composition of the samples was explored by EDX (Bruker Nano GmbH, Berlin, Germany, detector: XFlash 7100, window: slew AP3.3, thickness = 0.45 mm, Si dead layer = 0.029 µm) on the SEM instrument at an accelerating voltage of 5 kV and a measurement time of 2000 s. For TEM grid preparation, the sample was dispersed in ethanol and sonicated to achieve a uniform suspension. A small volume of the dispersion was then carefully deposited onto a TEM-grid and dried at room temperature. The

TEM imaging was done with an accelerating voltage of 100 kV. Solid state NMR measurements were recorded on Bruker ZAF (av400-zaf) (probe: PH MAS 400WB BL4 N-P/F-H DVT) spectrometers, where the chemical shifts are reported in ppm. NMR measurements for liquid samples were recorded on Bruker (av400e-ac) (probe: PA BBO 400S1 BBF-H-D-05 Z SP) spectrometers in D_2O and DMSO-d_6. The chemical shifts are reported in ppm and are referenced against the residual solvent signal. Prior to physisorption experiments, the samples were activated under vacuum at 120 °C overnight. Nitrogen physisorption isotherms were measured at 77 K on a Quadrasorb SI from Quantachrome Instruments. The specific surface area was determined *via* quenched solid density functional theory (QSDFT) kernel for carbons (slit/ cylindrical/ spherical pores) on the adsorption branch. X-ray photoelectron spectra (XPS) were recorded using an X-ray photoelectron spectrometer (Thermo Scientific, Kα) equipped with a monochromatic Al Kα X-ray source (hv = 1486.6 eV). For XPS measurements, the powder samples were pressed onto an adhesive Cu foil. During the measurement, a flood gun, which was calibrated to the C=C bond at 284.8 eV in PE, was used for charge compensation. For compositional data, survey spectra were measured with a step size of 1 eV and a pass energy of 100 eV. Valence band (VB) spectra were recorded in the binding energy range from −5 eV to 40 eV with a step size of 0.2 eV, a pass energy of 50 eV and a total of 20 scans. The high-resolution C 1s, N 1s and O 1s spectra were recorded with a step size of 0.05 eV, a pass energy of 30 eV and 5 scans each. The VB positions determined from VB-XPS are referenced to the work function of the XPS spectrometer rather than the absolute vacuum level. Therefore, the absolute VB and CB potential (E_{VB} and E_{CB}) values include the instrumental reference. However, as all samples were measured under identical instrumental conditions and calibration, the relative shifts in band edges between g-C_3N_5 and AR-CQD/g-C_3N_5-N_v remain accurate, reliable, and meaningful for comparing their photocatalytic energy-band structure.

Steady-state UV/vis absorption and emission spectroscopy

The steady-state absorption spectra were recorded using a Jasco-V780 UV-vis-NIR spectrophotometer in 1 cm quartz cuvettes. Steady-state emission spectra were recorded using an FLS980 fluorescence spectrometer (Edinburgh Instruments Ltd, the United Kingdom) equipped with a 450 W ozone-free xenon arc lamp as the excitation source. Emission spectra were collected using 1 cm quartz cuvettes, with excitation wavelengths ranging from 320 to 500 nm in 20 nm increments. The spectral slit widths were set to 2 nm for excitation and 3 nm for emission channels, respectively. g-C_3N_5, CQD, and the g-C_3N_5/CQD heterojunction with a concentration of 1 g L^{-1} were prepared from the respective stock solutions to measure steady-state absorption. Steady-state emission measurements were conducted on all samples normalized to an optical density of 0.1 at 320 nm to ensure consistent excitation conditions.

Photothermal deflection spectroscopy (PDS)

The photothermal deflection spectroscopy (PDS)[8-10] setup used here consists of a light source (LOT-QD, 1000 W Xe high-pressure lamp and a 300 mm monochromator (LOT-QD MSH 300) optimized for a maximum intensity of 200 nm to 2500 nm). The light is modulated by a chopper (Thorlabs) with a frequency of 5 Hz and focused on a spot size of 2 × 6 mm on the sample through a f = 75 mm lens. The intensity of the incident light (250 nm: 2.9-6.5 µW, 265 nm: 9.9-12.7 µW, 275 nm: 14.7 µW, 410 nm: 90 µW, 1100 nm: 174 mW) is monitored using a

quartz glass plate as a beam splitter placed between the focusing lens and the sample, and a trans-impedance amplified silicon detector (Thorlabs). The deflection of a 0.5 mW HeNe laser (LINOS, λ = 633 nm, HeNe 633-0.8-PO, beam diameter of 0.49 mm) is measured with a lateral effect sensor (Thorlabs PDA90). The deflection and reference signals were read out using two lock-in amplifiers (Stanford Research Systems SRS-830). The whole system is controlled by a self-written Labview program, which collects all data and also corrects the PDS signal according to the incident light intensity. A glassy carbon plate (3 mm × 30 mm) was used as a reference sample. The samples – thin films on quartz glass – were fixed in the center of a quartz glass cuvette (CV10Q3500F, Thorlabs) filled with FC-40 (Sigma Aldrich). The PDS measurement was carried out from 200 nm to 900 nm in 4 nm steps, with the monochromator slits adjusted to 3.2 mm, yielding a spectral resolution of 8 nm in the wavelength range of 200-1000 nm.

UV-vis diffuse reflectance spectroscopy (DRS)

UV-vis diffuse reflectance spectroscopy (DRS) measurements of the prepared films out of the g-C_3N_5, AR-CQDs, and AR-CQDs/g-C_3N_5 solutions were performed using a Jasco V-780 UV-vis-NIR spectrophotometer equipped with an integrating sphere in the wavelength range 200-800 nm. $BaSO_4$ powder was used as a reflectance standard.

Time-resolved transient absorption spectroscopy

Femtosecond transient absorption (TA) measurements were carried out using a custom-built setup operated at room temperature.[11] A white-light supercontinuum probe was generated by focusing a small fraction of the output from an amplified Ti:Sapphire laser system (Libra, Coherent; 1 kHz repetition rate) onto a rotating CaF_2 crystal. The resulting white-light continuum was split into a probe and reference beam. The probe was then focused onto the sample contained in a 1 mm quartz cuvette using a concave mirror with a 500 mm focal length. Probe and reference spectra were recorded using a Czerny-Turner spectrograph (SP2150, Princeton Instruments; 150 mm focal length) equipped with a diode array detector (Pascher Instruments AB, Sweden). Pump pulses at 320, 400, and 480 nm with a pulse duration of ~100 fs was generated using a non-collinear optical parametric amplifier (NOPA, TOPAS-White). The average pump power was set to 200 µW, corresponding to an estimated fluence of 71 µJ cm^{-2}. The repetition rate of the pump beam was reduced to 0.5 kHz using a mechanical chopper, and the relative polarization between the pump and probe beams was set to the magic angle (54.7°) to eliminate polarization-dependent artifacts. After passing through the sample, the pump beam was blocked, and the probe intensity was recorded as a function of the temporal delay between the pump and probe pulses, with time delays accessible up to 2 ns. Prior to analysis, the TA data were chirp-corrected using the coherent artifact signal.[12] The data analysis was obtained using a KimoPack software tool and global kinetic analysis was subsequently performed by using a consecutive fitting model at a confidence level of 95%.[13]

Photoelectrochemical measurements

The transient photocurrent response and electrochemical impedance spectroscopy (EIS) measurements were conducted using a Zahner electrochemical workstation (Zennium-ECW, Thales XT) equipped with a three-electrode configuration. For the preparation of the working

electrode, 5 mg of the synthesized sample was dispersed in 2 mL of ethanol and ultrasonicated for 1 hour to achieve a homogeneous dispersion. Subsequently, 0.1 mL of the resulting slurry was deposited onto an FTO glass substrate using a spin-coating system (SCC-200). The coated substrates were then dried at 120 °C for 6 hours to ensure proper adhesion and stability, after which they were used as the working electrode. A platinum electrode was utilized as the counter electrode, and an Ag/AgCl electrode served as the reference electrode. The electrolyte, consisting of a 0.2 M Na_2SO_4 solution, was degassed with N_2 gas prior to measurements to remove dissolved oxygen, ensuring optimal electrochemical performance. EIS spectra were recorded over a frequency range of 0.1 Hz to 100 kHz, and a 300 W Xenon lamp was employed as the light source for photoelectrochemical experiments.[14]

Photocatalytic CO_2 reduction experiments

The CO_2 photocatalytic reduction performance was evaluated at ambient temperature. For the experiments, 5 mg of the AR-CQDs/g-C_3N_5 photocatalyst was uniformly suspended in 5 mL of a MeCN/H_2O (4:1) solution containing triethanolamine (10% TEOA) as a hole-sacrificial agent, in a glass vial. The reaction was irradiated by blue LED light source (500 mW, Thorlabs, M455L3-C1, λ = 455 nm), positioned 5 cm vertically away, with a total volume of approximately 20 mL under continuous stirring. Before the formal experiments, the solution was purged with N_2 gas to remove any dissolved gases, followed by 40 minutes of purging with high-purity CO_2 (99.99%). Samples were taken periodically throughout the irradiation process and the produced gas analyzed using a gas chromatograph (GC) (Agilent Technologies, 7820A) equipped with a thermal conductivity detector (TCD). Liquid products were analyzed by ^{1}H NMR and GC-MS (Rt-Q-Bond column, 30 m × 0.32 mm inner diameter × 10 um film thickness, Serial #648311) with an MS ion source at a temperature of 200°C. The peak area of the product acetaldehyde (CH_3CHO) was correlated with a standard calibration curve of CH_3CHO for quantitative analysis. GC-TCD analysis of the gaseous phase detected trace amounts of H_2 and CO along with oxygen as minor byproducts during the photocatalytic reduction of CO_2 in this study. Product selectivity toward CH_3CHO was calculated from calibrated GC analysis as the molar fraction of acetaldehyde relative to the total amount of quantified carbon-containing products. For isotope-labeling studies, $^{13}CO_2$ was used instead of $^{12}CO_2$, and gaseous products were analyzed with a GC-MS system (GCMS-QP2020, Shimadzu) equipped with HS-20 headspace sampler. Helium was used as the carrier gas during the measurement. All the photocatalytic reactions were repeated three times to confirm the reliability of the data. No products were detected when N_2 was used in place of CO_2 under the same conditions, confirming that CO_2 was the source of CH_3CHO. To test reusability, N_2 gas was passed through the system after each of the five cycles to remove any residual CO_2 molecules from the catalyst surface.[4]

Photocatalytic H_2 evolution experiments

The photocatalytic hydrogen evolution reaction (HER) was performed at room temperature in a glass vial under blue LED light. In a standard procedure, 5 mg of AR-CQDs/g-C_3N_5 photocatalyst was dispersed in a 10% TEOA solution with constant stirring. Before the reaction, the vial was sealed and purged with N_2 gas to eliminate any residual O_2. Following this, the suspension was irradiated with the blue LED (500 mW, Thorlabs, M455L3-C1, λ = 455 nm), positioned 5 cm vertically away, to evaluate H_2 generation. H_2 gas was collected at 1-hour intervals and analyzed using a GC (Agilent Technologies, 7820A) with a TCD.

Statistical Analysis

Statistical methods, including data presentation and sample sizes, were provided in the corresponding figure and table captions.

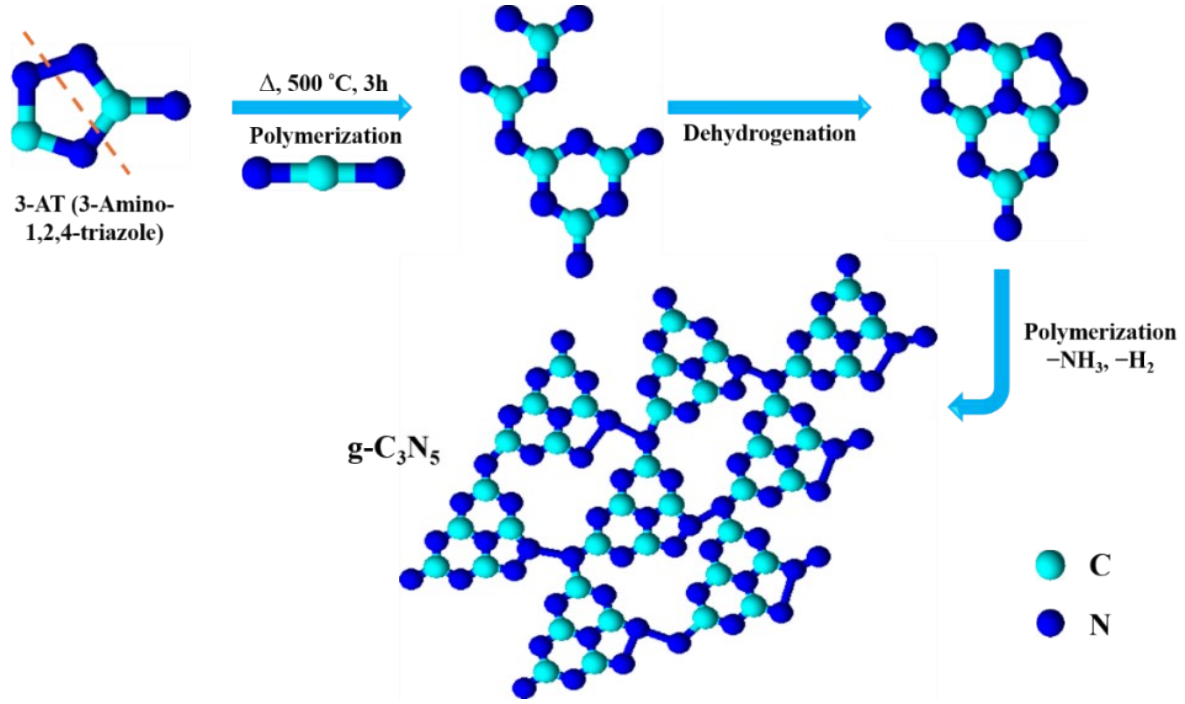

Scheme S1. Plausible mechanism of the formation of g-C_3N_5.[1]

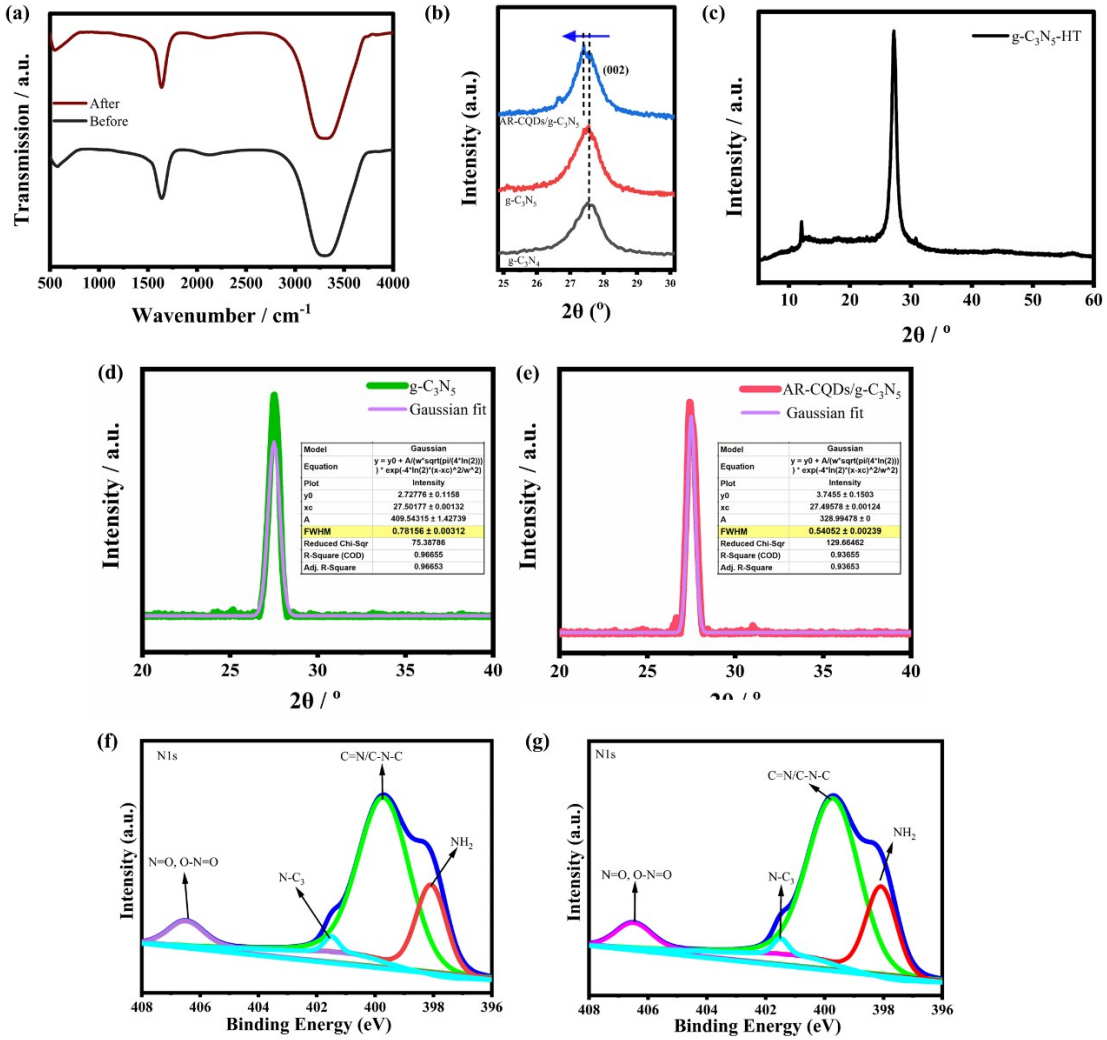

Figure S1. (a) FTIR evidence for the chemical stability of AR-CQDs under hydrothermal conditions. FTIR spectra of AR-CQDs recorded before and after hydrothermal treatment performed under the same conditions used for hybrid preparation. The spectra show no appreciable changes in the characteristic vibrational bands, indicating that the overall surface functional-group motif of the AR-CQDs is largely preserved under the applied hydrothermal conditions. (b) XRD patterns. (c) XRD of the process control g-C_3N_5-HT (ultrasound/hydrothermal treatment without AR-CQDs) shows only the characteristic (100)/(002) reflections and no feature at around 6.1°, indicating that the low-angle reflection observed in the hybrid is AR-CQDs-associated rather than an effect of hydrothermal processing alone. Gaussian fitting parameters of XRD patterns of (d) g-C_3N_5 and (e) AR-CQDs/g-C_3N_5 within 20° and 40° shows a narrower full width at half maximum (FWHM) in case of AR-CQDs/g-C_3N_5. (f–g) High-resolution N 1s XPS spectra of AR-CQDs recorded before (f) and after (g) hydrothermal treatment. The spectra were deconvoluted into components corresponding to amine (–NH_2), C=N/C–N–C, N–C_3, and oxidized nitrogen species. Notably, the –NH_2-associated signal at 398 eV remains clearly present after hydrothermal treatment, with no evident shift in binding energy, consistent with the retention of amino functionalities under the applied conditions.

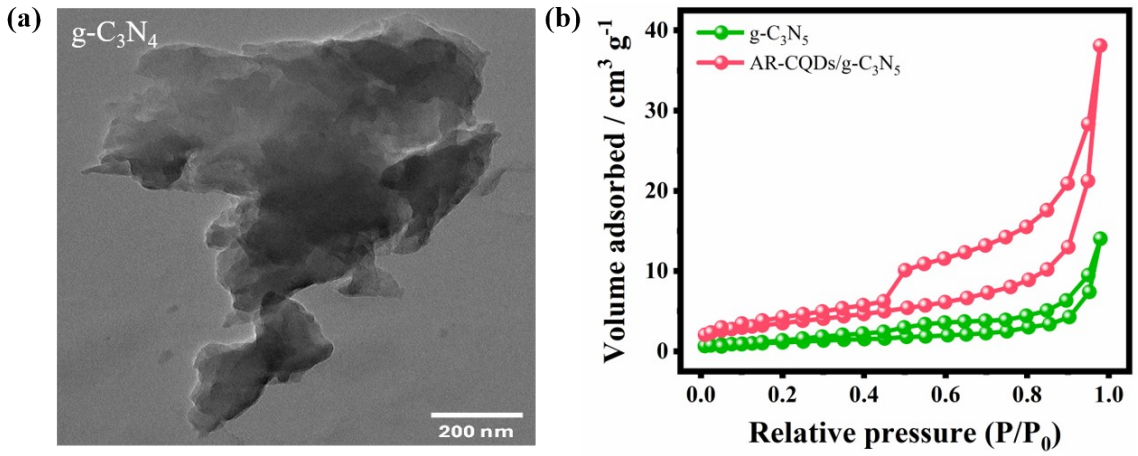

Figure S2. (a) TEM image of conventional g-C_3N_4. (b) Nitrogen physisorption isotherms of g-C_3N_5 and AR-CQDs/g-C_3N_5.

Note: Fig. S2b shows higher N_2 adsorption for AR-CQDs/g-C_3N_5, consistent with processing-induced loosening of stacked g-C_3N_5 and an increased specific surface area.

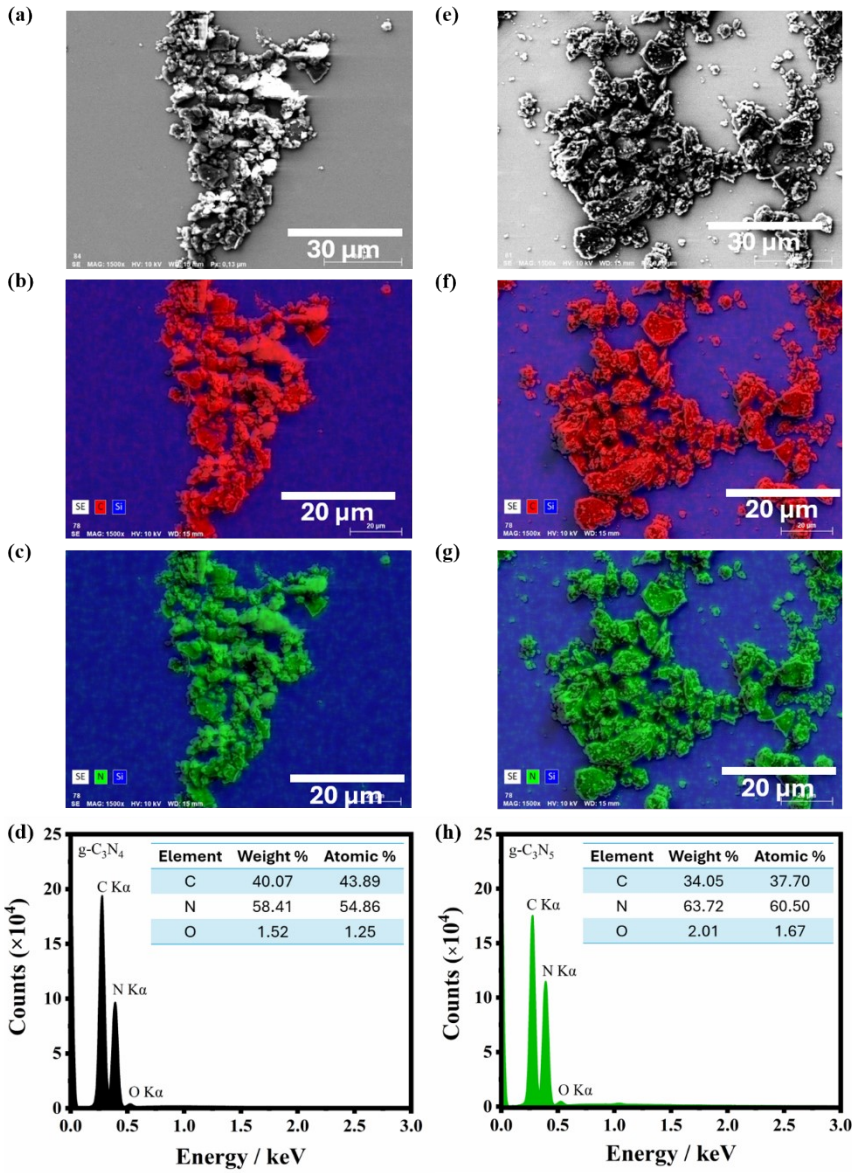

Figure S3. (a-c) EDS mapping images of conventional g-C_3N_4. (d) EDX spectra of conventional g-C_3N_4. The inset shows the elemental composition. (e-g) EDS mapping images of bulk g-C_3N_5. (h) EDX spectra of bulk g-C_3N_5. The inset shows the elemental composition.

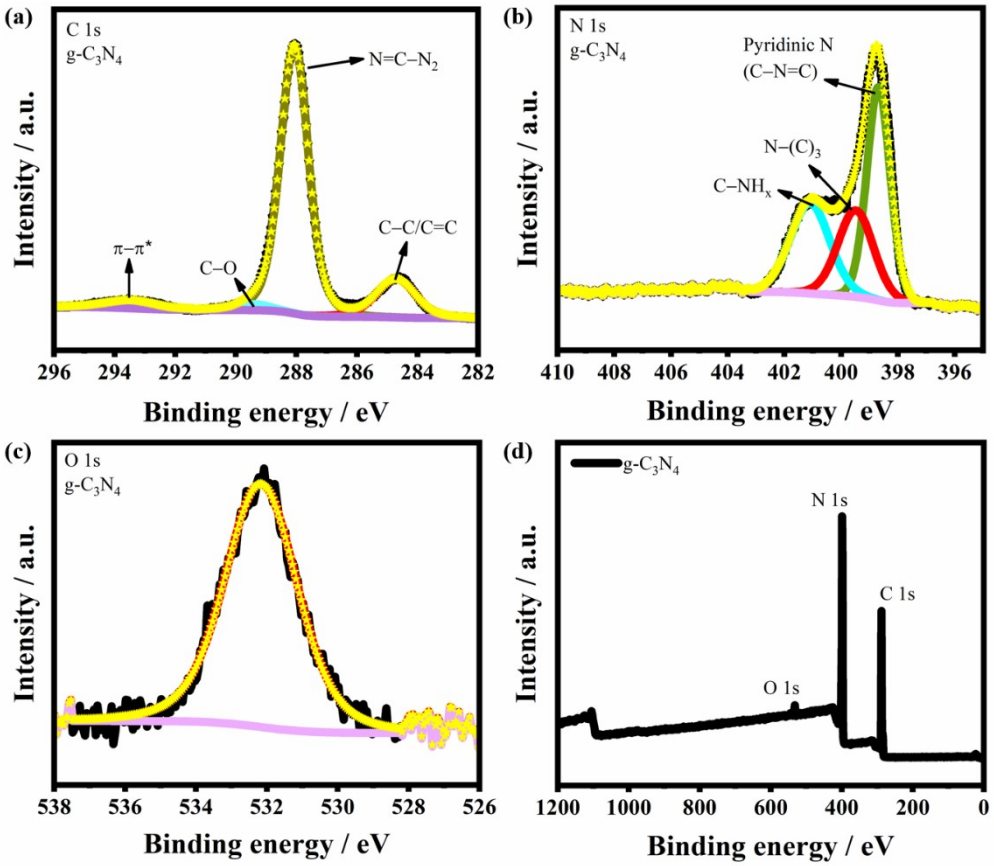

Figure S4. XPS spectra of conventional g-C_3N_4[3]: (a) C 1s, (b) N 1s, (c) O 1s, and (d) Survey.

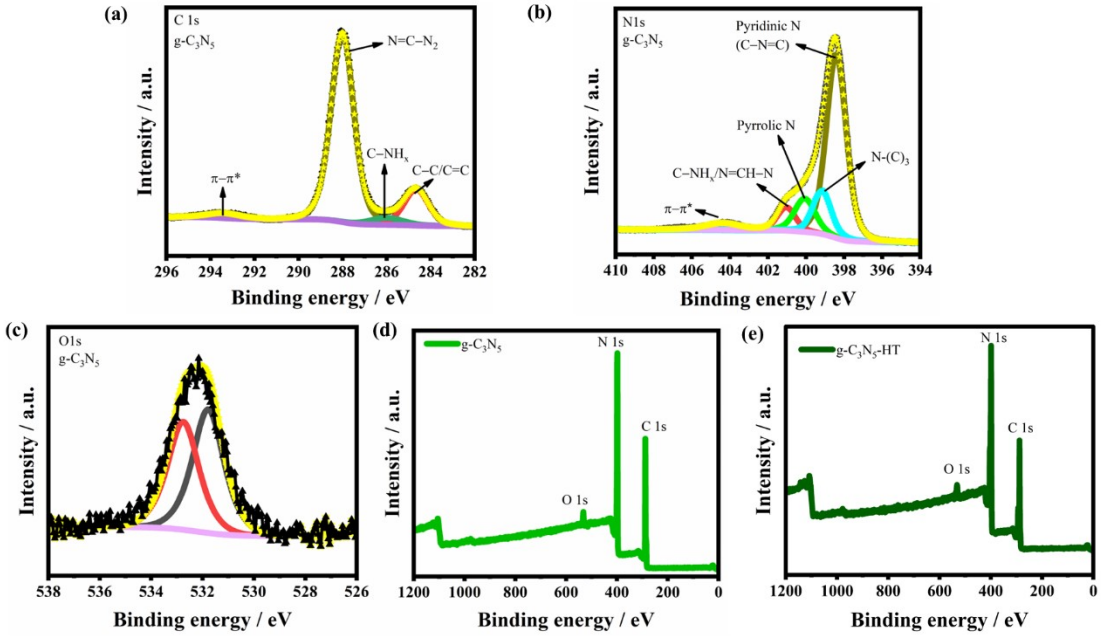

Figure S5. XPS spectra of g-C_3N_5 photocatalyst: (a) C 1s, (b) N 1s, (c) O 1s. Survey XPS spectrum of g-C_3N_5 (d) and AR-CQDs/g-C_3N_5 (e).

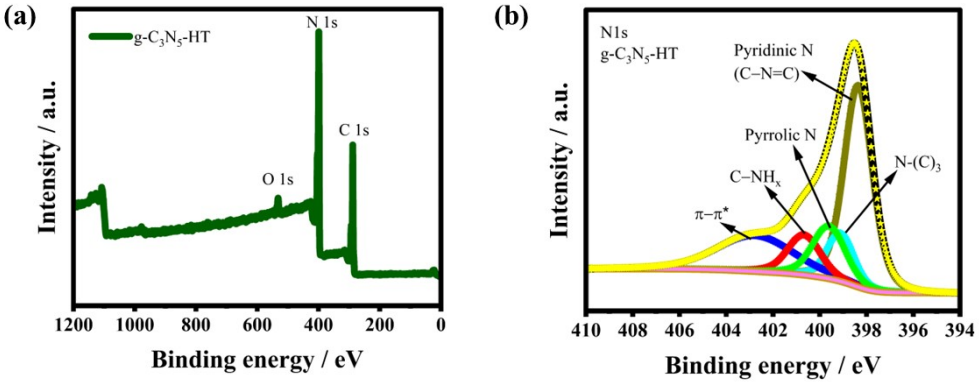

Figure S6. XPS spectra of the process-matched hydrothermal control g-C_3N_5-HT: (a) XPS survey spectrum showing the presence of C, N and O. (b) High-resolution N 1s spectrum with peak deconvolution into Pyridinic N (N_2C), N–$(C)_3$ (N_3C), pyrrolic N, C–NH_X, and a high-binding-energy shake-up (π–π–type) contribution.

Observation (process-matched control): To assess whether the ultrasound/hydrothermal treatment alone induces vacancy-like changes in g-C_3N_5, we prepared a process-matched control sample g-C_3N_5-HT under identical conditions but without AR-CQDs. The high-resolution N 1s XPS spectrum of g-C_3N_5-HT shows an N_2C/N_3C peak-area ratio of 4.42, which is essentially unchanged compared with pristine g-C_3N_5 (4.52). In contrast, AR-CQDs/g-C_3N_5 exhibits a markedly lower N_2C/N_3C ratio (2.39). These results indicate that the hydrothermal/ultrasound treatment alone does not produce the vacancy-like change in N_2C/N_3C; instead, the change emerges specifically during AR-CQDs-assisted coupling.

Table S1. Relative percentage of different peaks from N 1s XPS spectra of synthesized photocatalysts.

Catalysts	Pyridinic N (N_{2C})	N–$(C)_3$ (N_{3C})	Pyrrolic N	C–NH_X / N=CH–N	π–π*	N_{2C}: N_{3C}
g-C_3N_4	398.6 eV (42.84 %)	399.4 eV (26.50 %)	–	401.1 eV (30.63 %)	–	1.61
g-C_3N_5	398.4 eV (62.69 %)	399.1 eV (13.89 %)	400.6 eV (11.95 %)	401.0 eV (7.30 %)	404.3 eV (4.17 %)	4.52
AR-CQDs/ g-C_3N_5	398.4 eV (52.26 %)	399.0 eV (21.79 %)	399.9 eV (13.47%)	400.9 eV (8.66 %)	404.7 eV (3.82 %)	2.39

Table S2. Relative percentage of different peaks from C 1s XPS spectra of synthesized photocatalysts.

Catalysts	N=C−(N)$_2$	C−C / C=C	C−NH$_X$	O=C−O	π−π*
g-C_3N_4	288.0 eV (78.10 %)	284.7 eV (15.71 %)	–	289.3 eV (1.95 %)	293.3 eV (4.24 %)
g-C_3N_5	288.0 eV (77.14 %)	284.6 eV (15.81 %)	286.0 eV (3.98 %)	–	293.3 eV (3.06 %)
AR-CQDs/ g-C_3N_5	288.2 eV (76.55 %)	284.8 eV (16.89 %)	286.0 eV (3.63 %)	–	293.7 eV (2.93 %)

Table S3. Calculated band gap and associated electronic properties, *e.g.*, mid-gap states, valence and conduction band potentials of the synthesized photocatalysts.

Catalysts	Band gap (E_g) (in eV)	Mid-gap states (E_{MGSs}) (in eV)	E_{VBM} (in eV)	E_{CBM} (in eV)	E_{CBM} of mid-gap states (in eV)
g-C_3N_4	2.78	–	1.74	−1.04	–
g-C_3N_5	2.09	–	1.62	−0.47	–
AR-CQDs[7]	2.81	–	2.02	−0.79	–
AR-CQDs/ g-C_3N_5	2.46	2.13	1.71	−0.75	−0.42

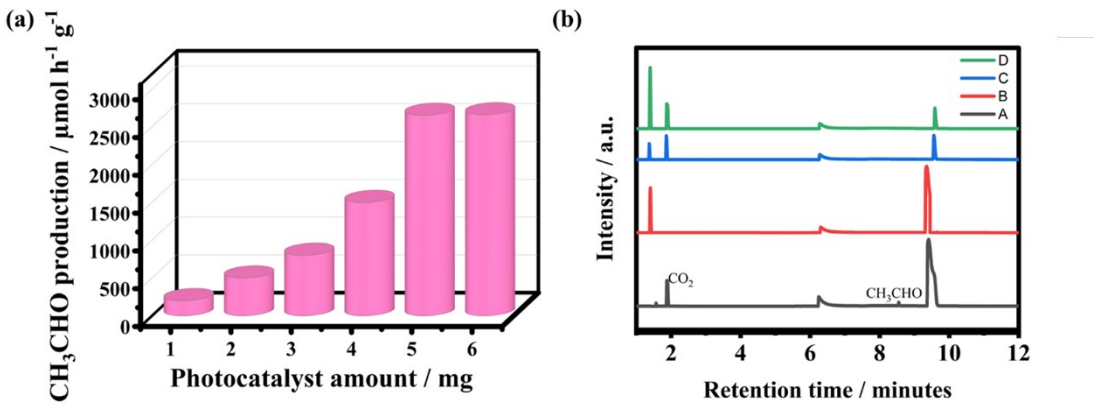

Figure S7. (a) Product (CH_3CHO) yield variation as a function of the catalyst quantity. (b) Control GC–MS experiments addressing the origin of acetaldehyde in the presence of TEOA. Representative GC–MS total ion chromatograms (TIC) of the products obtained under the same experimental setup: (A) CO_2 + light + photocatalyst + TEOA (full reaction), (B) N_2 + light + photocatalyst + TEOA (CO_2-free control), (C) CO_2 + dark + photocatalyst + TEOA (light-off control), and (D) CO_2 + light + TEOA (photocatalyst-free control). The acetaldehyde peak at around 8.2 min (verified using an external CH_3CHO standard) is observed only in (A) and is absent in controls (B–D). These controls indicate that, under the applied conditions, CH_3CHO is not produced from TEOA oxidation, supporting CO_2-dependent formation. Note: Chromatograms are vertically offset for clarity; peak positions and relative intensities are preserved.

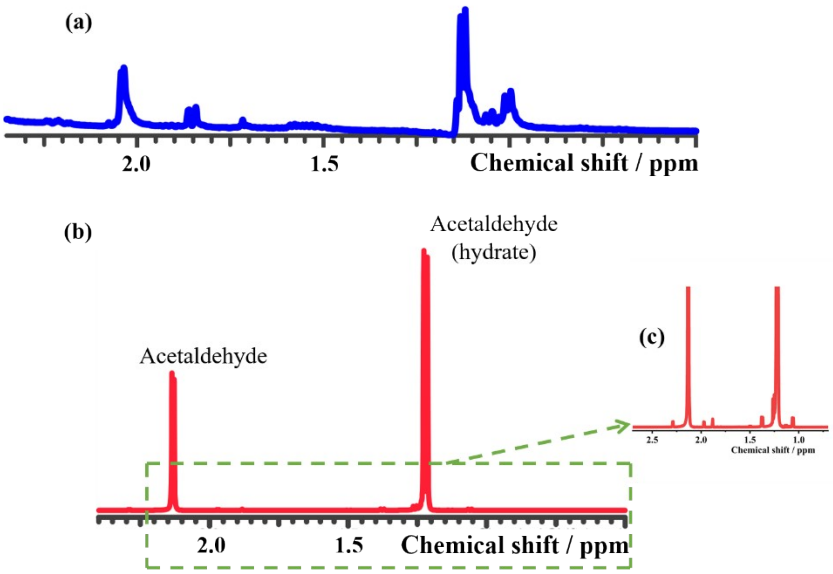

Figure S8. (a) ^1H NMR spectra of reaction mixture after 10 hours of visible light irradiation under optimized conditions in 0.4 mL D_2O. The spectra qualitatively support the formation of acetaldehyde. (b) ^1H NMR spectra of standard CH_3CHO aqueous solution (Note: the liquid sample is stored at 10 °C before using the NMR analyzed with water suppression). (c) Enlarged view of the 1.7–2.0 ppm region from the standard CH_3CHO aqueous solution spectrum, highlighting minor spectral features associated with solution-phase equilibria (e.g., hydrate formation). Comparable features are also observed in the reaction mixture, indicating that these signals can arise from solution-phase equilibria rather than significant formation of additional byproducts.

Table S4. A comparative analysis of photocatalytic performance of various reported photocatalysts for CO_2 conversion into CH_3CHO product in representative studies.

Serial No.	Photocatalysts	Light source	CH_3CHO (μmol h^{-1} g^{-1})	CH_3CHO selectivity (%)	References
1	Janus Ag/AgClBr	AM 1.5G, 100 mW cm^{-2}	209.3	96.9	*Nanoscale*, 2021, **13**, 20289
2	C-doped SnS_2 nanostructures	300 W halogen lamp	96.7	85	*Nat. Commun.*, 2018, **9**, 169
3	Pd/Rh/TiO_2 nanoparticles	320-500 nm, 41.62 mW cm^{-2}	0.21	70.9	*Appl. Catal. B*, 2012, **126**, 172
4	foam-like Cu_2O	UV-vis light	8.2	–	*Sol. Energy*, 2016, **139**, 452.
5	g-C_3N_4/CuO@MIL-125(Ti)	simulated sunlight, 32.61 mW cm^{-2}	177.2	16.5	*Chem. Eng. J.*, 2020, **399**, 125782
6	Nb-doped TiO_2 nanotube array	simulated solar illumination	572	100	*ACS Appl. Mater. Interfaces*, 2020, **12**, 55982
7	ultrafine $ZnFe_2O_4$ nanoparticles	visible light	57.8	–	*J. Mater. Sci. Technol.*, 2018, **34**, 2331.
8	NiO/$InTaO_4$ layer	AM 1.5G, 100 mW cm^{-2}	0.3	88.5	*Energy Environ. Sci.*, 2011, **4**, 1487

9	$SnS\text{-}SnS_2$ nanosheets	AM 1.5G, 100 mW cm^{-2}	11.5	31.5	*ACS Appl. Mater. Interfaces*, 2021, **13**, 4984
10	Rb/K co-modified carbon nitride	AM 1.5G, 100 mW cm^{-2}	1212.3	93.3	*Angew. Chem.*, 2023, **135**, e202218720
11	**Metal-free AR-CODs/g-C_3N_5**	**Blue LED**	**2653**	**95.2**	**This work**

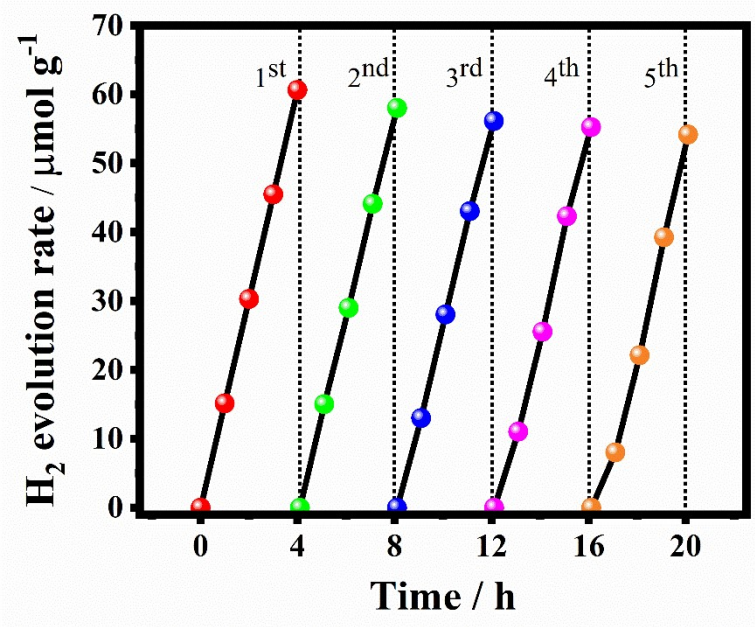

Figure S9. Stability evaluation through recycling experiments for H_2 production using AR-CQDs/g-C_3N_5.

Note: We note a slightly lower cycling stability under HER conditions, which may reflect differences in solvent composition (aqueous TEOA vs MeCN/H_2O) and the associated surface hydration/stacking behaviour of carbon nitride during repeated irradiation.[15]

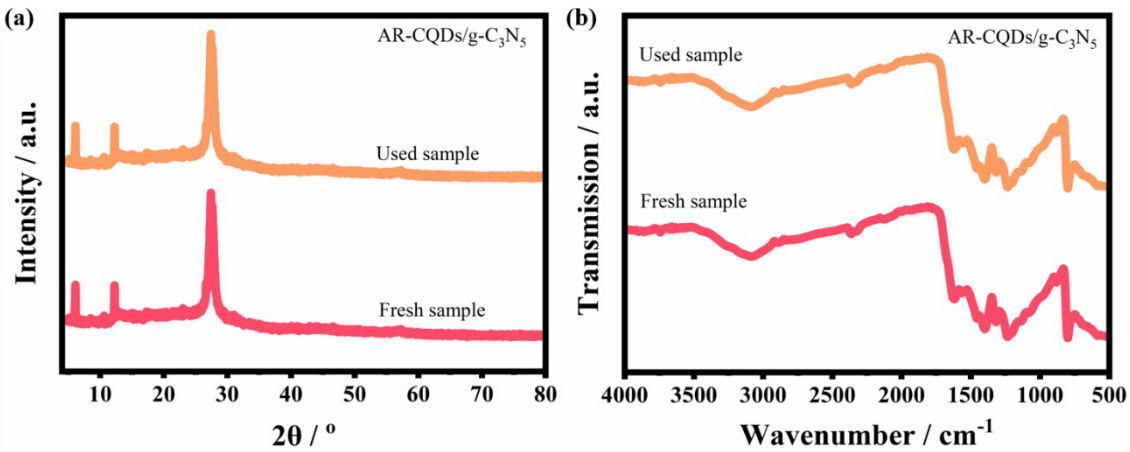

Figure S10. (a) XRD patterns and (b) FTIR spectra of fresh and used AR-CQDs/g-C_3N_5 for photocatalytic CO_2 reduction.

Note S1. Steady-State Spectroscopy

We begin the discussion with the steady-state absorption and emission data of g-C_3N_5, AR-CQDs, and the AR-CQDs/g-C_3N_5 shown in Figure S11. g-C_3N_5 (green line) exhibits two prominent absorption bands in the UV region (*ca.* 230-350 nm), corresponding to π-π* transitions within the conjugated units of the g-C_3N_5 framework (Figure S11a). The weaker absorption between 350 and *ca.* 500 nm is attributed to n-π* transitions involving nitrogen lone-pairs and structural defects like nitrogen vacancies. The broad absorption extending into the visible region of nitrogen-rich g-C_3N_5 is in line with literature[16,17] and reflects the narrower bandgap of the material (*ca.* 2.1 eV) compared to conventional g-C_3N_4 (*ca.* 2.7 eV). AR-CQDs (blue line) absorb strongly in the UV due to π-π* transitions of sp^2-hybridized C=C bonds as reflected in the rather strong absorption at *ca.* 230-300 nm (Figure S11a). Additionally, AR-CQDs also exhibit a weak absorption primarily arising from n-π* transitions associated with the surface functional groups, extends into the visible region (*ca.* 300-500 nm).[18] The absorption spectrum of the AR-CQDs/g-C_3N_5 (red line) contains features of both pristine g-C_3N_5 and AR-CQDs (Figure S11a) and maintains strong UV absorption between *ca.* 200-350 nm. Additionally, AR-CQDs/g-C_3N_5 retains significant visible-light absorption, characteristic of g-C_3N_5, implying that the intrinsic optical properties of g-C_3N_5 are not disturbed by the AR-CQDs. To gain additional insight into surface-associated optical features, we conducted photothermal deflection spectroscopy (PDS) on thin films of g-C_3N_5, AR-CQDs, and AR-CQDs/g-C_3N_5. As shown in Figure S12, the normalized PDS spectra of all three samples closely resemble their UV-vis absorption profiles, confirming the reliability of both techniques in capturing key optical transitions. Pristine g-C_3N_5 exhibits strong absorption up to *ca.* 500 nm with a distinct shoulder in the visible region, while AR-CQDs primarily absorb in the UV with a gradual decay into the visible range. Notably, AR-CQDs/g-C_3N_5 retains the broad absorption features of g-C_3N_5, including its visible-light tail. The close agreement between PDS, which indirectly probes pristine absorption and can even detect weak absorption,[19,20] and steady-state absorption measurements confirms that the optical modifications induced by AR-CQDs integration are consistent throughout the film and accessible at the interface.

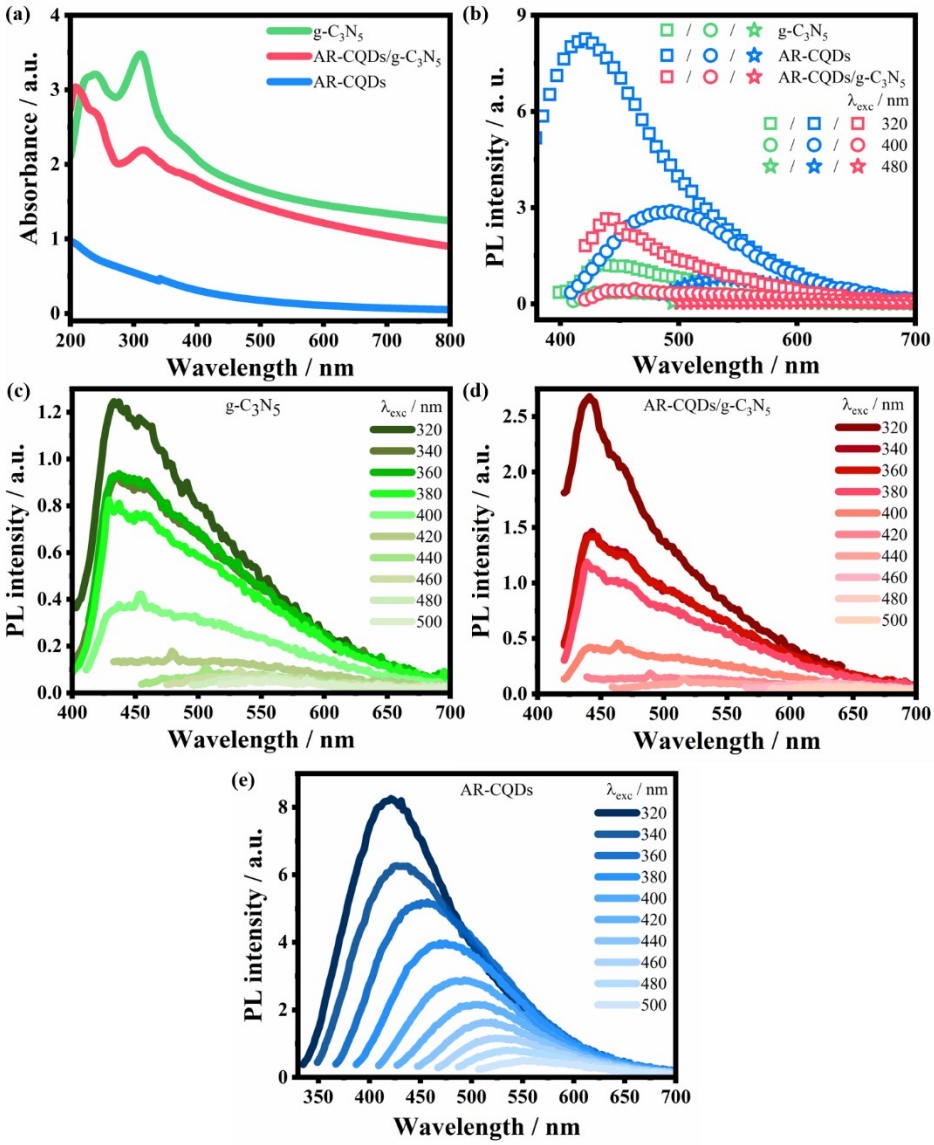

Figure S11. (a) Steady-state absorption behavior of g-C_3N_5 (green), AR-CQDs (blue), and AR-CQDs/g-C_3N_5 (red). (b) Photoluminescence spectra of g-C_3N_5 (green), AR-CQDs (blue), and AR-CQDs/g-C_3N_5 (red) recorded at particular excitation wavelengths of 320, 400, and 480 nm. Steady-state photoluminescence spectra of (c) g-C_3N_5, (d) AR-CQDs/g-C_3N_5, and (e) AR-CQDs upon varying excitation wavelengths from 320 to 500 nm.

The photoluminescence (PL) of g-C_3N_5, AR-CQDs, and AR-CQDs/g-C_3N_5 upon various wavelength excitation are summarized in Figure S11b and a full account of the data is given in Figure S11c-S11e. Figure S11b depicts the corresponding PL spectra of pristine g-C_3N_5 (green), AR-CQDs (blue), and AR-CQDs/g-C_3N_5 (red) upon excitation at 320 (square), 400 (circle), and 480 nm (star). Irrespective of the excitation wavelengths, g-C_3N_5 shows an emission peak at 435 nm.[21] The emission of the AR-CQDs/g-C_3N_5 peaks at slightly longer wavelengths, *i.e.*, at 440 nm, pointing towards slightly altered energetics of the emissive states at the AR-CQDs/g-C_3N_5 interface. AR-CQD displays broad PL features extending from 400 to 620 nm with varying emission peaks between 420 to 550 nm (Figure S11e). Such broad PL likely arises from surface defect states.[22-24] This emission of such defects is typically excitation wavelength-dependent,[25-26] and dominate at shorter wavelengths (320-380 nm),

and give rise to high PL intensities. The comparably intense emission of the AR-CQDs/g-C_3N_5 upon excitation between 320-380 nm (Figure S11d) originates from surface states of AR-CQDs.[22-24] The weaker emission upon excitation at 400-500 nm reflects features of both g-C_3N_5 and AR-CQDs/g-C_3N_5. At longer excitation wavelengths, where absorption of AR-CQDs is minimal, the PL of AR-CQDs/g-C_3N_5 closely reflects that of pristine g-C_3N_5, indicating that the observed emission originates from g-C_3N_5.

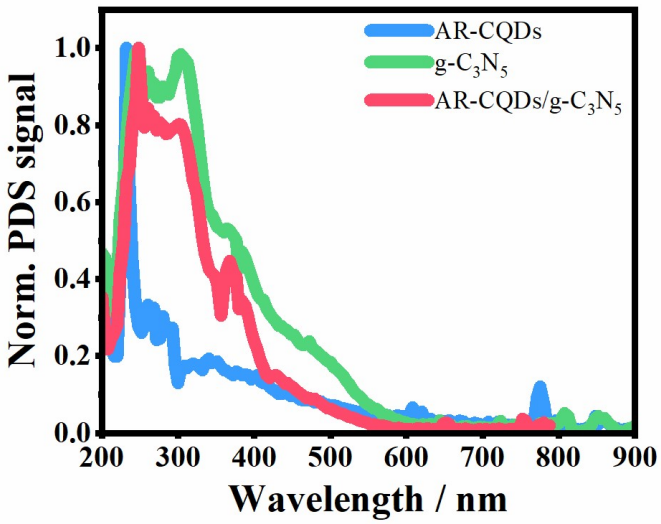

Figure S12. Photothermal deflection spectra (PDS) of drop-casted thin films of AR-CQDs, g-C_3N_5, and AR-CQDs/g-C_3N_5 deposited on quartz substrates. The sharp peak at 232 nm for the AR-CQDs is most likely arising from the underlying quartz glass substrate. The data are normalized to the maximum absorbance value, which occurs at 248 nm for g-C_3N_5 and the AR-CQDs/g-C_3N_5, and at 232 nm for AR-CQDs.

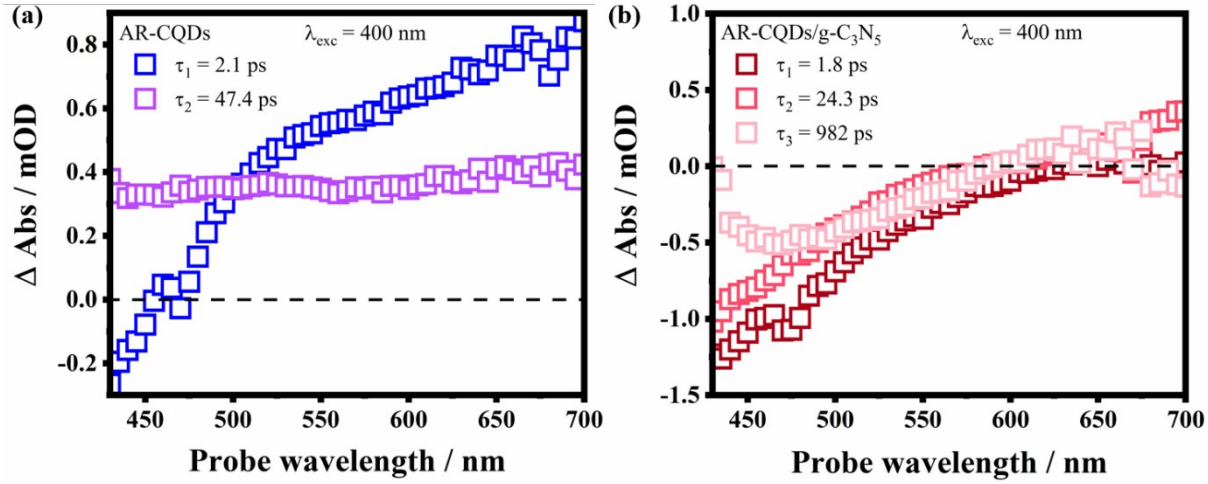

Figure S13. Decay associated spectra (DAS) of (a) AR-CQDs and (b) AR-CQDs/g-C_3N_5 in the wavelength range of 430-700 nm obtained from global kinetic fit.

Note S2. Transient Absorption Spectroscopy of g-C_3N_5, AR-CQDs/g-C_3N_5, and AR-CQDs under 320 and 480 nm Excitation

At 320 nm excitation, AR-CQDs displays a broad ESA band across 450-650 nm (Figure S14a), which dominates at early delay times and progressively weakens at longer delays as a result

of excited carrier recombination or trapping. The absence of GSB is consistent with their UV absorption, while weak negative signals at the ns-timescale may arise from stimulated emission of emissive states. Similar to 400 nm, the kinetic behavior of AR-CQDs shows biexponential dynamics, this time with a fast component around 0.3 ps and a slower component around 27 ps (Figure S14b). Despite differences in characteristic time constants compared to 400 nm excitation – particularly evident in the faster sub-picosecond (*ca.* 0.3 ps at 320 nm versus *ca.* 2 ps at 400 nm) and the slower component (*ca.* 27 ps at 320 nm versus *ca.* 47 ps at 400 nm) – the fundamental photophysical relaxation mechanism remains consistent. The ultrafast (sub-picosecond) relaxation at 320 nm likely results from rapid internal conversion processes involving higher excited states initially populated upon excitation at 320 nm. The comparatively shorter lifetimes at 320 nm thus reflect an increased rate of intraband relaxation and internal conversion processes. Meanwhile, the slower decay components consistently reflect carrier trapping dynamics involving defect or surface states.[28,29] Thus, the differences in absolute lifetime values arise primarily due to excitation-energy-dependent variations in initial excited-state populations and subsequent internal relaxation pathways, rather than fundamental differences in the nature of the relaxation processes themselves.

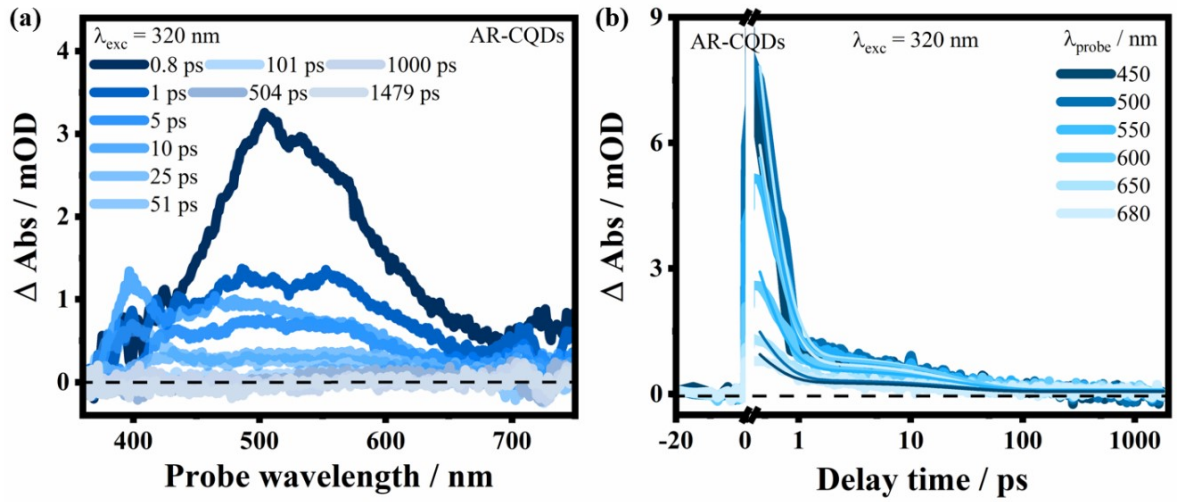

Figure S14. (a) fs-TA spectra of AR-CQDs upon 320 nm excitation. (b) TA decay kinetics of AR-CQDs upon 320 nm excitation. The solid lines within the TA data represent corresponding global fits.

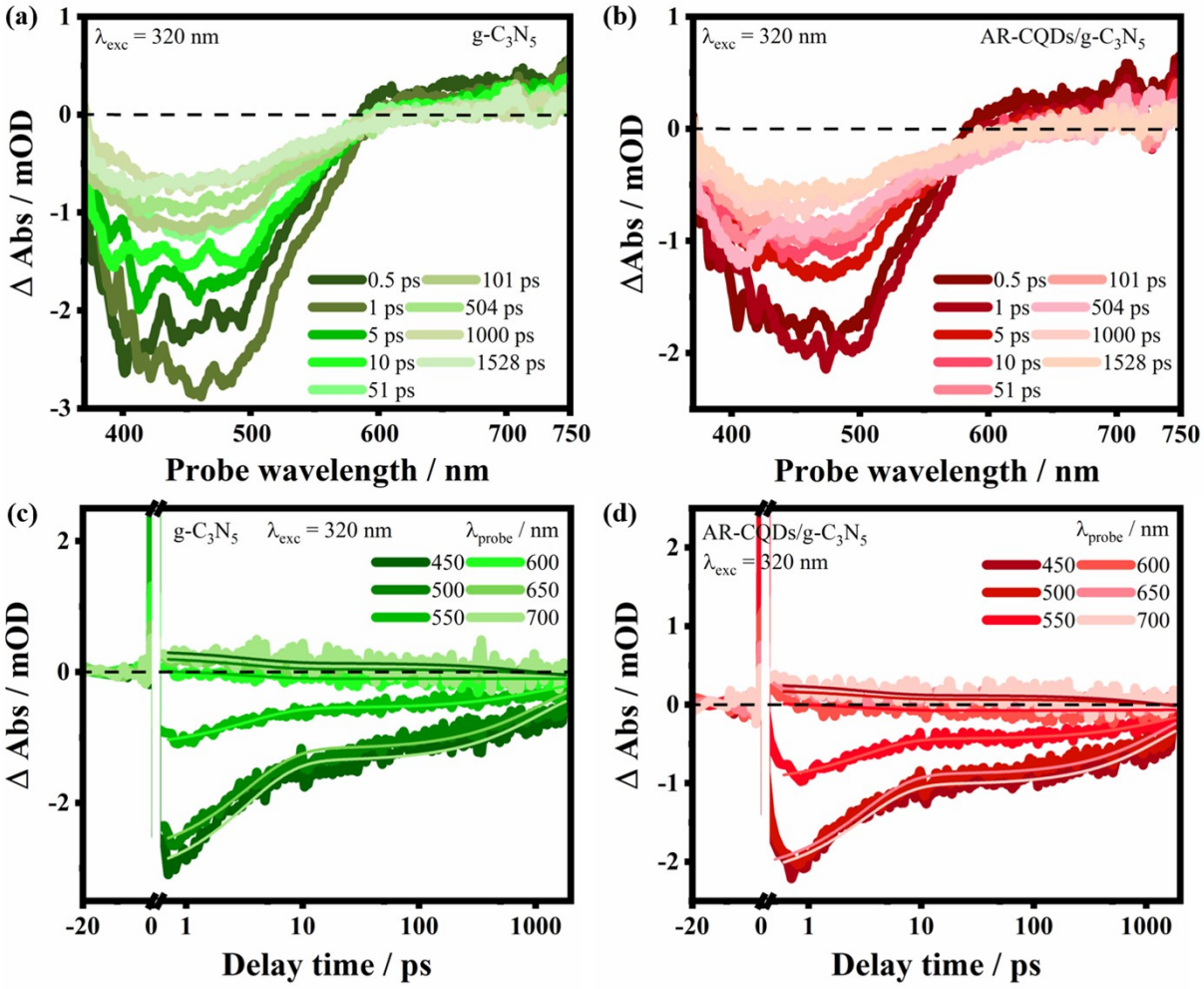

Figure S15. fs-TA spectra of (a) g-C_3N_5 and (b) AR-CQDs/g-C_3N_5 with a concentration of 0.5 mg mL^{-1} at 320 nm excitation. TA decay kinetics of (c) g-C_3N_5 and (d) AR-CQDs/g-C_3N_5 at 320 nm excitation. The solid lines within the TA data represent corresponding global fits.

Upon excitation at 320 nm, the fs-TA spectra of both pristine g-C_3N_5 and AR-CQDs/g-C_3N_5 exhibit similar spectral evolution (Figure S15a and S15b). A GSB between 370 and 600 nm is accompanied by an ESA beyond *ca.* 600 nm. The minimal spectral differences between AR-CQDs/g-C_3N_5 and g-C_3N_5 suggest a negligible influence of the photoexcited AR-CQDs on the excited-state dynamics excited at 320 nm. While steady-state PL data upon 320-nm excitation show modest emission enhancement in AR-CQDs/g-C_3N_5, these effects likely stem from static contributions such as defect passivation or additional emissive states associated with AR-CQDs. However, they do not manifest as interfacial charge transfer within the ultrafast regime probed by TA spectroscopy. Therefore, despite overlapping UV absorption, the AR-CQDs contribution to the initial carrier relaxation remains limited at 320 nm excitation, consistent with the nearly identical fs-TA signatures of AR-CQDs/g-C_3N_5 and g-C_3N_5. First, we consider the kinetic analysis of the TA data of g-C_3N_5 and AR-CQDs/g-C_3N_5 recorded upon 320 nm excitation based on a global analysis (Figure S15c and S15d). The decay kinetics of g-C_3N_5 followed a biexponential decay with characteristic time constants $\tau_1 \approx 3.3$ ps and $\tau_2 \approx 1.1$ ns. For AR-CQDs/g-C_3N_5, a very similar fast decay ($\tau_1 \approx 3.1$ ps) and a comparable longer-lived component ($\tau_1 \approx 1.4$ ns) to g-C_3N_5 were observed. The fast component is associated with intrinsic exciton relaxation processes within the g-C_3N_5 structure, such as rapid exciton

diffusion and localization to shallow defect states, while the longer component corresponds to exciton recombination dynamics involving deeper trap states, such as nitrogen-vacancy defect sites. The very close resemblance of the time constants and spectral signatures in both g-C_3N_5 and AR-CQDs/g-C_3N_5 indicates that the presence of AR-CQDs at this excitation wavelength neither significantly alters the intrinsic exciton relaxation nor allows for interfacial electron transfer within the ultrafast timescale probed here.

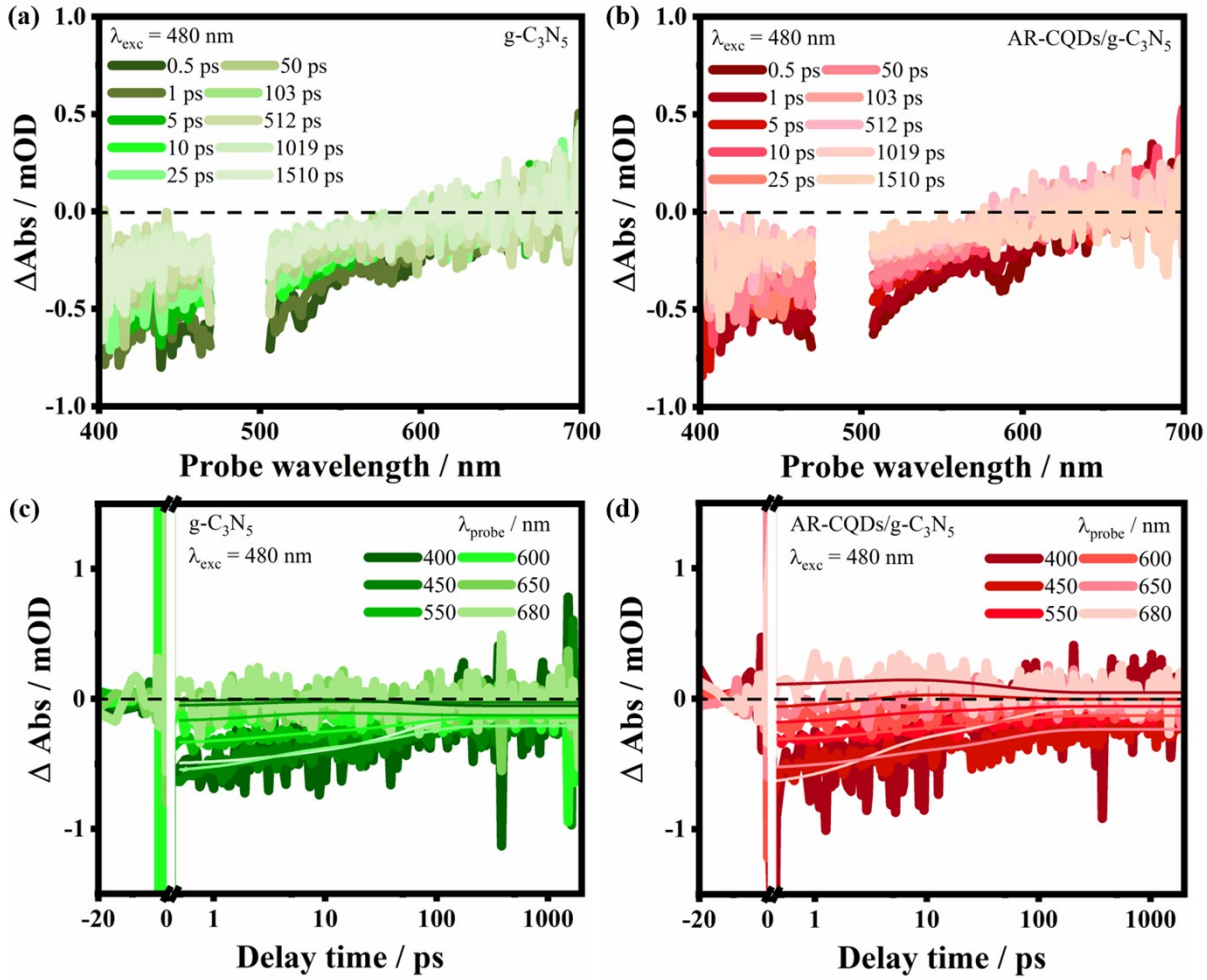

Figure S16. fs-TA spectra of (a) g-C_3N_5 and (b) AR-CQDs/g-C_3N_5 with a concentration of 0.5 mg mL^{-1} at 480 nm excitation. TA decay kinetics of (c) g-C_3N_5 and (d) AR-CQDs/g-C_3N_5 at 480 nm excitation. The solid lines within the TA data represent the corresponding global fits.

To complete the excitation-dependent fs-TA studies, g-C_3N_5 and AR-CQDs/g-C_3N_5 were excited at 480 nm. The fs-TA spectra of both g-C_3N_5 and AR-CQDs/g-C_3N_5 exhibited overall similar features (Figure S16a and S16b). A GSB appeared prominently within the spectral region of *ca.* 400-600 nm. Beyond 600 nm, no ESA was distinguishable, indicating that conduction band electrons or shallow trap states in g-C_3N_5 are not populated efficiently under these excitation conditions. Furthermore, kinetic analysis within the bleach region revealed comparable dynamics for both the g-C_3N_5 and AR-CQDs/g-C_3N_5 (Figure S16c and S16d). The kinetics are accounted for by two characteristic time constants, *i.e.*, 2.8 and 55 ps for g-C_3N_5 and 3 and 50 ps for AR-CQDs/g-C_3N_5. We associate the two corresponding processes with fast

exciton relaxation and charge trapping and point out that the negligible difference between the TA data obtained for both materials indicates the absence of effective electron transfer from the AR-CQDs to g-C_3N_5 upon excitation at 480 nm. This observation can be rationalized by considering the significantly lower absorption cross-section of AR-CQDs at this wavelength, rendering them insufficiently excited and unable to undergo oxidative quenching and subsequent electron injection into g-C_3N_5.

Table S5. A comparative analysis of the characteristic time constants obtained from the TA datasets of AR-CQDs, g-C_3N_5, and AR-CQDs/g-C_3N_5 upon excitation at 320, 400, and 480 nm. These characteristic time constants have been obtained *via* global fitting of the decay kinetics of the materials at respective wavelengths.

Materials	λ_{exc} = 320 nm	λ_{exc} = 400 nm	λ_{exc} = 480 nm
AR-CQDs	τ_1 = 0.27 ± 0.01 ps τ_2 = 26.6 ± 1.1 ps	τ_1 = 2.1 ± 0.1 ps τ_2 = 47.4 ± 0.7 ps	–
g-C_3N_5	τ_1 = 3.3 ± 0.1 ps τ_2 = 1094 ± 192 ps	τ_1 = 6.1 ± 0.2 ps τ_2 = 213.8 ± 12.6 ps	τ_1 = 2.8 ± 0.2 ps τ_2 = 54.9 ± 3.8 ps
AR-CQDs/g-C_3N_5	τ_1 = 3.1 ± 0.1 ps τ_2 = 1412 ± 195 ps	τ_1 = 1.8 ± 0.2 ps τ_2 = 24.3 ± 2.9 ps τ_3 = 982 ± 176 ps	τ_1 = 3.2 ± 0.3 ps τ_2 = 50 ± 4.3 ps

References

1 Z. Li, Y. Zhou, Y. Zhou, K. Wang, Y. Yun, S. Chen, W. Jiao, L. Chen, B. Zou, M. Zhu, *Nat. Commun.*, 2023, **14**, 5742.

2 S. Rajendran, T. Chellapandi, V. UshaVipinachandran, D. V. Ramanaiah, C. Dalal, S. K. Sonkar, G. Madhumitha, S. K. Bhunia, *Appl. Surf. Sci.*, 2022, **577**, 151809.

3 A. Dandia, P. Saini, K. Kumar, M. Sethi, K. S. Rathore, M. L. Meena, V. Parewa, *Curr. Res. Green Sustainable Chem.*, 2021, **4**, 100170.

4 K. Kumar, P. Saini, M. Sethi, S. Saini, A. Gurjar, A. Konar, B. Dietzek-Ivanšić, W. Weigand, V. Parewa, *ACS Appl. Mater. Interfaces*, 2024, **16**, 43498.
5 S. Saini, P. Saini, K. Kumar, M. Sethi, P. Meena, A. Gurjar, A. Dandia, T. Dhuria, V. Parewa, *ACS Appl. Mater. Interfaces*, 2023, **15**, 49083.
6 S. Saini, K. Kumar, P. Saini, M. Sethi, P. Meena, A. Dandia, W. Weigand, V. Parewa, *ACS Appl. Mater. Interfaces*, 2024, **16**, 46200.
7 S. Meena, M. Sethi, S. Saini, K. Kumar, P. Saini, S. Meena, S. Kashyap, M. Yadav, M. L. Meena, A. Dandia, N. K. Nirmal, V. Parewa, *J. Colloid Interface Sci.*, 2024, **660**, 756.
8 M. Presselt, F. Herrmann, S. Shokhovets, H. Hoppe, E. Runge, G. Gobsch, *Chem. Phys. Lett.*, 2012, **542**, 70.
9 A. Asano, M. Stutzmann, *J. Non-Cryst. Solids*, 1991, **137-138**, 623.
10 M. L. Hupfer, F. Herrmann-Westendorf, B. Dietzek, M. Presselt, *Analyst*, 2021, **146**, 5033.
11 R. Siebert, D. Akimov, M. Schmitt, A. Winter, U.S. Schubert, B. Dietzek, J. Popp, *ChemPhysChem*, 2009, **10**, 910.
12 B. Dietzek, T. Pascher, V. Sundström, A. Yartsev, *Laser Phys. Lett.*, 2007, **4**, 38.
13 C. Müller, T. Pascher, A. Eriksson, P. Chabera, J. Uhlig, *J. Phys. Chem. A*, 2022, **126**, 4087.
14 H. Chen, C. Lim, T. Tan, M. Zhou, L. Zhang, X. Sun, Z. He, Y. Ye, X. Li, H. Zhang, J. W. Han, C. Yang, Y. Chen, *ACS Nano*, 2023, **17**, 10677.
15 M. Xiao, M. Lyu, Z. Wang, L. Wang, *ChemSusChem*, 2024, **17**, 202400937.
16 J. Zhang, Z. Li, J. He, H. Tao, M. Chen, Y. Zhou, M. Zhu, *ACS Catal.*, 2023, **13**, 785.
17 W. Chu, Z. Qiao, J. Wu, Z. Zhu, C. Gong, H. Huang, P. He, T. Cui, S. Chen, M. Lin, *Energy Mater Adv.*, 2023, **4**, 0064.
18 Y. Deng, M. Chen, G. Chen, W. Zou, Y. Zhao, H. Zhang, Q. Zhao, *ACS Omega*, 2021, **6**, 4247.
19 F. Herrmann, S. Engmann, M. Presselt, H. Hoppe, S. Shokhovets, G. Gobsch, *Appl. Phys. Lett.*, 2012, **100**, 153301.
20 W. J. D. Beenken, F. Herrmann, M. Presselt, H. Hoppe, S. Shokhovets, G. Gobscha, E. Runge, *Phys. Chem. Chem. Phys.*, 2013, **15**, 16494.
21 S. Qin, L. Huang, Y. Zhang, T. Zhang, M. Tian, J. Jiang, *Sci. Rep.*, 2025, **15**, 787.
22 H. Shabbir, E. Csapó, M. Wojnicki, *Inorganics*, 2023, **11**, 262.
23 Y. Han, L. Liccardo, E. Moretti, H. Zhao, A. Vomiero, *J. Mater. Chem. C*, 2022, **10**, 11827.
24 Y. Dong, R. Wang, H. Li, J. Shao, Y. Chi, X. Lin, G. Chen, *Carbon*, 2012, **50**, 2810.
25 Y.-P. Sun, B. Zhou, Y. Lin, W. Wang, K. A. S. Fernando, P. Pathak, M. J. Meziani, B. A. Harruff, X. Wang, H. Wang, P. G. Luo, H. Yang, M. E. Kose, B. Chen, L. M. Veca, S.-Y. Xie, *J. Am. Chem. Soc.*, 2006, **128**, 7756.
26 H. Li, X. He, Z. Kang, H. Huang, Y. Liu, J. Liu, S. Lian, C. H. A. Tsang, X. Yang, S.-T. Lee, *Angew. Chem., Int. Ed.*, 2010, **49**, 4430.

27 S. Zhu, Q. Meng, L. Wang, J. Zhang, Y. Song, H. Jin, K. Zhang, H. Sun, H. Wang, B. Yang, *Angew. Chem., Int. Ed.*, 2013, **52**, 3953.
28 X. Wen, P. Yu, Y.-R. Toh, X. Hao, J. Tang, *Adv. Optical Mater.*, 2013, **1**, 173.
29 B. Gao, G. Hartland, T. Fang, M. Kelly, D. Jena, H. G. Xing, L. Huang, *Nano. Lett.*, 2011, **11**, 3184.